Performance Enhancing of Galloping-based Piezoelectric Energy Harvesting by Exploiting 1:1 Internal Resonance of Magnetically Coupled Oscillators

Wan Sun
Jiangsu University
Canzhi Guo
Jiangsu University
Guanggui Cheng
Jiangsu University
Shangwen He
Zhengzhou University
zhaorui yang (zryang@zzu.edu.cn)
Zhengzhou University
Jianning Ding
Jiangsu University

Research Article

Keywords: Internal resonance, Multiple time scale, Frequency synchronization, Nonlinear force coupling, Wind energy harvesting

Posted Date: November 3rd, 2021

DOI: https://doi.org/10.21203/rs.3.rs-1022013/v1

Performance enhancing of galloping-based piezoelectric energy harvesting by exploiting 1:1 internal resonance of magnetically coupled oscillators

Wan Sun[a,b], Canzhi Guo[a,b], Guanggui Cheng[a,b], Shangwen He [b], Zhaorui Yang[b]*, Jianning Ding [a,b]*

[a] Institute of Intelligent Flexible Mechatronics, Jiangsu University, Zhenjiang 212013, P.R. China

[b] Jiangsu Collaborative Innovation Center of Photovoltaic Science and Engineering, Changzhou University, Changzhou 213164, P.R. China

[c] School of Mechanics and Safety Engineering, Zhengzhou University, Zhengzhou 450001, P.R. China

*Corresponding Author

E-mail address:

zryang@zzu.edu.cn (Zhaorui Yang)

dingjn@ujs.edu.cn (Jianning Ding)

Abstract

In this study, we introduced 1:1 internal resonance in a magnetically coupled 2-degree-of-freedom (2-DOF) galloping-based piezoelectric energy harvester to improve the energy harvesting efficiency. The governing equations for the proposed magnetically coupled aero-electro-mechanical system considering the effect of oscillating wake are established using the extended Hamilton principle, and the method of multiple scale is exploited to obtain approximate analytical solutions. Parameter sweeping numerical calculation is conducted to validate the analytical prediction through comparing with analytical solutions, and the results show a good matching between them. In addition, we investigated the systematic dynamic behaviors under a pure oscillating wake induced 1:1 internal response. Typical nonlinear characteristics such as jump, hysteresis, frequency synchronization under varying design parameters appear in the present system. Especially, cusp bifurcation and synchronization regime of oscillating wake coupled nonlinear oscillator in $\eta-\Theta_w$ plane and $\sigma-\Theta_w$ plan. With an adoption of magnetic force, chaos happens as the gap distance decreases smaller than 5 mm, and a frequency lock-in phenomenon can be strengthened through adjusting the magnet distance. In the perspective of output performance, both of the voltage and power output results shows that the exploiting of 1:1 internal resonance can significantly improve the output performance under a suitable magnet distance.

Keyword: Internal resonance; Multiple time scale; Frequency synchronization; Nonlinear force coupling; Wind energy harvesting.

1 Introduction

With the dramatic increasing of energy consumption due to the rapid industrial development, a series of environmental pollution problems have been continually arisen over the past few decades. It is anticipated that the development of renewable and sustainable energy is the trend of human development in the future, and this viewpoint is becoming the consensus all over the world. Energy harvesting from the surrounding environment as an alternative of renewable energy has been receiving increasing interest in recent few decades. In particular, the recent rapid developments of wireless sensor networks necessitate some new demands on self-powering technologies such as portability, small-scale, high efficiency, environmental adaptability, which promotes numerous researchers devoting their efforts in developing various energy harvesting technologies.

In accordance with the operation environment of the sensor nodes and electric devices, various forms of wasted energy sources such as wind [1], mechanical [2, 3], thermal, solar, and chemical sources can be selected and converted into electric energy for the electric consumption devices. Wind energy, as one of the most common wasted energy sources, which has abundant free utilization value. A large amount usage of wind energy has been applied to the traditional rotating wind turbine [4, 5] for commercial power supplies because of its high output and high efficiency in wind energy conversion. On the other hands, wind turbine is difficult to meet the requirements of self-power supply of small-scale wireless sensors that need a compact structural integration of the power supply components and target small-scale electric device. Therefore, the instinct shortage of the wind turbine applying in small-scale electric devices accelerated the development of the studies on compact wind energy harvesting

system based on flow induced vibrations such as vortex-induced vibration (VIV), galloping, flutter, and wake galloping. Among them, galloping phenomenon is a representative flow-induced vibration, which happens when the structural system loses its stability. The galloping phenomenon is broadly applied in a small-scale wind energy harvesting system because it usually exhibits a large oscillation amplitude and wide operating wind velocity range compared to VIV, flutter and wake galloping [6-8].

The wind energy can be converted into electric energy through three typical transduction mechanisms of electromagnetic, electrostatic, and piezoelectric. Among them, the piezoelectric mechanism is the most popular owing to its high energy density and easiness of application [8-10]. In the last decade, a variety of piezoelectric wind energy harvesters (PEH) have been studied from the basis mechanisms of flow induced vibration to the technologies of improving energy conversion efficiency [11-15]. Among various aerodynamic phenomenon-based wind energy harvesters, galloping-based piezoelectric wind energy harvester (GPEH) exhibits an excellent performance compared to the others because of its larger amplitude response and wider operational wind range. A general GPEH is composed of a cantilever beam attached with piezo patch and a cross-section asymmetric bluff body fixed on its free end. To further improve energy harvesting efficiency and reduce the critical wind speed, some researchers have been devoting their efforts on optimizing the cross-section of bluff body [16-21], exerting synergy effect by combining aerodynamic phenomena (VIV, galloping) [22-25] and increasing the degrees of freedom (DOF) [26, 27]. Lan et al. [26] proposed lumped parameter models for two structural configurations with different bluff bodies under aerodynamic force. They analytically and

numerically compared the output performances between the proposed configurations which shows that the second configuration with the wind flow loaded on the outer bluff body can easily and remarkably reduce the critical wind speed and improve the output power. In addition, Hu et al. [7] recently proposed a comb-like beam (CombBeam) based GPEH, which consists of several parasitic beams mounted on a conventional cantilever beam. This structure is regarded as a multiple-degree-of-freedom (MDOF) system. They showed that the MDOF CombBeam-based GPEH was superior to the conventional beam GPEH in reducing the cut-in wind speed from 2.24 m/s to 1.96 m/s and enhancing the power for about 171.2% with an optimal resistance under a specific wind speed of 3 m/s. Starting from such kinds of linear 2-DOF GPEH, an exploiting of external nonlinear force in a flow induced vibration energy harvester was also considered in some works to further enhance the energy harvesting performance. Wang et al. [28] proposed a double-beam piezo–magneto–elastic nonlinear wind energy harvester, in which two piezoelectric cantilever beams attached to prism-like bluff bodies employing repulsive magnets were fixed vertically and oriented to face each other. Most recently, Sun et al. [6] investigated a magnetically coupled GPEH in a tandem configuration to improve the energetic performance, which consists of two elastic structures with two bluff bodies and a pair of repulsive magnets installed for the generation of mutual interaction between them. This work showed that a maximum overall average output power of 8.09 mW and power improvement rate of 65% were obtained compared to the case without magnetic interaction under an optimal magnetic gap distance.

However, to the best of our knowledge, few study has reported on consideration of the effects of

the natural frequency ratio between the oscillators to the overall output performance in a two or multiple DOF GPEH. Up till now, some systematic studies on the internal resonance have been carried out on a general 2-DOF PEH in the previous works. In these previous works [29-32], the dynamical behaviors show dramatical changes when one of the natural frequencies is close to the other where internal resonance happens. Internal resonance has been extensively reported in external forced vibration energy harvesting system for an output performance enhancement [33, 34], which usually appears when the ratio between two natural frequencies of a given system is close to an integer and various interesting phenomena such as frequency or (and) lock-in (synchronization), hysteresis, chaotic behaviors can be resulted in. Inspired by these work on internal resonance in a 2-DOF PEH, this study tried to exploit 1:1 internal resonance in a development of magnetically coupled galloping-based piezoelectric energy harvester (MCR- GPEH) for a significant output performance improvement.

This study proposed a lumped parameter model for the MCR-GPEH considering the effect of oscillating wake using Hamilton principle, and a series of comprehensive parametric studies have been analytically and numerically conducted to predict the evaluation of the symmetric dynamic behavior when the internal resonance happens. This work provides a general framework and design guidance for a high efficiency wind energy harvester by exploiting 1:1 internal resonance through controlling the distance. Both of the numerical and analytical results showed that 1:1 internal resonance wind energy harvesting system is expected to be a promising alternative in the development of high-efficiency galloping-based wind energy harvesting system.

2 Dynamic modeling

2.1 Conceptual description

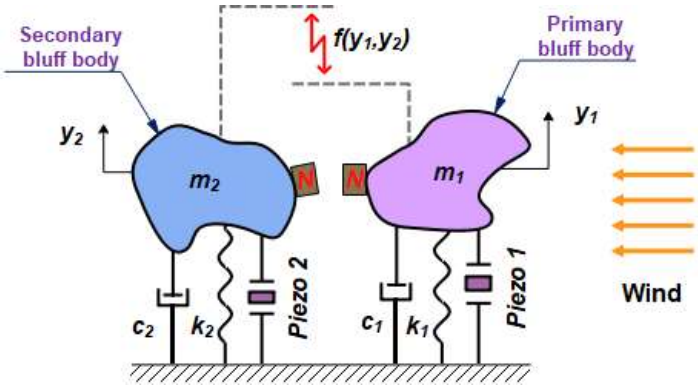

Fig. 1 Schematic of the magnetically coupled 2-DOF galloping-based piezoelectric energy harvester.

Conventional piezoelectric wind energy harvester based on galloping or VIV aerodynamic phenomenon is generally designed with a single cantilever beam and a bluff body fixed on its free end. The wind energy can be converted into structural vibration energy, and then into electric energy through the piezoelectric transducer, which has been thoroughly investigated in various aspects such as fundamental theory construction, novel structure design and aerodynamic energy conversion mechanism in the previous studies.

In this study, we proposed a magnetically coupled 2-DOF galloping-based piezoelectric energy harvester to increase the energy harvesting efficiency through double-steps energy extraction from the incoming wind flow using the tandem arrangement of the bluff bodies as shown in Fig. 1. The proposed structure is configured with two presumed arbitrary bluff bodies and individually connected to a fixture using elastic component. Considering the merits of galloping phenomenon in wind energy harvesting as

introduced in Introduction section, the cross-section shape of the bluff bodies is designed as circular asymmetric shape for aerodynamic instability. The primary bluff body is arranged in the front of the secondary bluff body with a tandem configuration along the wind incoming direction. The wind flow passing the primary bluff body generates wake flow that applies to the secondary bluff body and further give rise to the variation of its dynamic behaviors. However, the oscillation of the secondary bluff body has a negligible influence to the primary bluff body due to the directionality of the wake flow as investigated in [35]. In this study, we exploited a pair of mutually repelling magnets, which are attached to the inner side of each bluff body to strengthen the coupling effect of the dynamic behaviors of the two bluff bodies to achieve synergistic effect.

This study focuses on the investigation of the overall output performance of the two individual elastic structures under various natural frequency difference. The nonlinear characteristics induced by the wind flow and magnet force lead to various nonlinear dynamic behaviors such as jump phenomenon, limit cycle, frequency synchronization and catastrophe bifurcation. The variation of the natural frequency difference between two weakly coupled mass-spring-damper system results in synchronization and internal resonance which is beneficial to improve the wind energy harvesting performance.

2.2 Governing equations

In this section, a mathematical modeling of the proposed magnetically coupled 2-DOF system is derived to predict the dynamic behaviors and output voltage performance. The proposed system consists

of two discrete mass-spring-damper components which are coupled with weak nonlinear magnetic force, the governing equations can be formulated using the expended Hamilton's principle as follows:

$$\int_{t_1}^{t_2} \left(\delta T_t - \delta \Pi_t + \delta W_{nc} \right) \mathrm{d}t = 0, \tag{1}$$

where t represents time, δT_t and $\delta \Pi_t$ represent the variations of the total kinetic and potential energy contained in this system, respectively, and δW_{nc} is the virtual work done by the non-conservative forces. The kinetic energy in the proposed system includes the translational and rotational kinetic energies of the outer and inner bluff bodies. Thus, the total kinetic energy T_t in the present system is given by

$$T_t = \frac{1}{2} m_1 \dot{y}_1^2 + \frac{1}{2} m_2 \dot{y}_2^2, \tag{2}$$

where the over-dot of a symbol denotes a derivative with respect to time t; m_1 and m_2 denote the total masses of the bluff bodies (primary, secondary) and the corresponding attached permanent magnets, respectively; y_1 and y_2 denote the displacement of the primary and secondary bluff bodies.

The potential energy of the proposed system includes several components such as the electrical, electromechanical, mechanical, and magnetic potential energy. Subsequently, the total potential energy Π_t of the proposed system is expressed as follows:

$$\Pi_t = U_{mag} + \frac{1}{2} k_1 y_1^2 + \frac{1}{2} k_1 y_2^2 - \frac{1}{2} c_{p1} \dot{\lambda}_1(t)^2 - \frac{1}{2} c_{p2} \dot{\lambda}_2(t)^2 - \theta_{e1} \dot{\lambda}_1(t) y_1 - \theta_{e2} \dot{\lambda}_2(t) y_2, \tag{3}$$

where k_1 and k_2 represent the spring constants of the primary and secondary spring; c_{p1} and c_{p2} represent the capacitance of the primary and secondary piezo components; θ_{e1} and θ_{e2} represent the piezoelectric coupling coefficients; $\dot{\lambda}_1$ and $\dot{\lambda}_2$ represent the flux linkage of the equivalent circuit of the

piezoelectric components; U_{mag} represents the potential energy from the magnetic field generated by the two repulsive magnets, which can be described by the dipole–dipole model due to the small size compared to the bluff body [36].

$$U_{mag} = -\frac{\mu_0}{4\pi}\left(\nabla \frac{\mathbf{m}_B \cdot \mathbf{r}_{BA}}{\left\|\mathbf{r}_{BA}\right\|_2^3}\right)\cdot \mathbf{m}_A = \frac{\mu_0}{4\pi}\left[\frac{1}{\left\|\mathbf{r}_{BA}\right\|_2^3}\mathbf{m}_B - \frac{3\left(\mathbf{m}_B \cdot \mathbf{r}_{BA}\right)}{\left\|\mathbf{r}_{BA}\right\|_2^5}\mathbf{r}_{BA}\right]\cdot \mathbf{m}_A, \tag{4}$$

where μ_0 is the vacuum permeability; $\mathbf{r}_{BA}$ is the vector from the center of the magnet A to the center of the magnet B; and $\mathbf{m}_A$ and $\mathbf{m}_B$ are the magnetic moment vectors of the outer and inner magnets, respectively. For a permanent magnet, the magnitude of the magnetization vector can be evaluated using the magnet's residual flux density B_r, that is, $\bar{m} = B_r / \mu_0$. Under a series of mathematical manipulation, the magnetic potential energy can be expressed as

$$U_{mag}(y_1, y_2) = -\frac{\bar{m}_1\bar{m}_2\bar{v}_1\bar{v}_2\mu_0}{4\pi}\left(y_{12}{}^2 + D_m{}^2\right)^{-1.5} - 3D_m{}^2\left(y_{12}^2 + D_m^2\right)^{-2.5}, \text{ with } y_{12} = y_1 - y_2, \tag{5}$$

referring to [6]. where $\bar{m}_1$ and $\bar{m}_2$ are the magnitudes of magnetization vectors, and $\bar{v}_1$ and $\bar{v}_2$ are the volumes of the primary and secondary magnets; and D_m is the minimum gap distance between the center points of the two magnets. Take the derivative with respect to y_{12} on the magnetic potential energy and then expand the resulting equation in a Taylor series at $y_{12} = 0$, the magnetic force can be obtained as

$$F_{mag} = \pm\left(\mathrm{T}_1 Y_{12} + \mathrm{T}_3 Y_{12}{}^3\right), \text{ with } \mathrm{T}_1 = -\frac{12\bar{m}_A\bar{m}_B\bar{v}_A\bar{v}_B\mu_0}{4\pi D_m^5}, \mathrm{T}_3 = \frac{45\bar{m}_A\bar{m}_B\bar{v}_A\bar{v}_B\mu_0}{4\pi D_m^7}. \tag{6}$$

The virtual work done by the non-conservative forces is given by

$$\delta W_{nc} = F_{g1}\delta y_1 + F_{g2}\delta y_2 + \theta_1^w \dot{y}_1 \delta y_2 + \theta_2^w \dot{y}_2 \delta y_1 + \delta y_1 - c_1 \dot{y}_1 \delta y_1 - c_2 \dot{y}_2 \delta y_2 - \dot{\lambda}_1(t)\delta\lambda_2(t)/R_{L2} - \dot{\lambda}_2(t)\delta\lambda_2(t)/R_{L2}, \tag{7}$$

where R_{L1} and R_{L2} represent the load resistances for the primary and secondary external circuit, respectively; c_1 and c_2 represent the damping constants; θ_i^w denote the wake force coefficients, and we assumed they are both equal to Θ_w; F_{g1} and F_{g2} are the aerodynamic transverse force acting on the bluff bodies, which can be expressed as [23]

$$F_{gi} = n_i U_i^2 C_{gi} \text{ with } n_i = 0.5\rho_a D H_i, \tag{8}$$

where the indices i =1, 2 represent the corresponding symbols for primary and secondary bluff bodies, respectively. ρ_a represents the air density; H_i and U_i are the height of the bluff bodies and the wind velocity applied to each bluff bodies. C_{gi} represents the dimensionless coefficients of the aerodynamic transverse force, which is a function of attack angle according to the assumption of quasi-steady state of the bluff bodies in wind flow field referring to the previous studies [19, 37]. C_{gi} is the inherent characteristics related to the cross-section shape of the bluff body and Renolds number, which can be obtained through series expansion of the transverse aerodynamic force at different rotation angles of the bluff body. It can be expressed as $C_{gi}(\alpha_i) = A_{1i}\alpha_i + A_{3i}\alpha_i^3 + A_{5i}\alpha_i^5 + \mathrm{L}$, with $\alpha_i = \dot{y}_i / U_i$, where A_{1i}, A_{3i}, A_{5i} are the aerodynamic coefficients. In this study, a third-order expansion is adopted to describe the nonlinear dynamic behaviors resulted from the aerodynamic force.

Subsequently, we performed several manipulations using variational calculus to Eqs. (2), (3) and (7), then substituted the resultants into Eq. (1) to gather the coefficients of δy_1, δy_2, $\delta\lambda_1(t)$ and $\delta\lambda_2(t)$.

Furthermore, we conducted a normalization manipulation for a calculation convenience, thus a set of governing equations can be obtained as

$$\ddot{y}_1 + \omega_1 y_1 + 2\omega_1\zeta_1\dot{y}_1 + \tau_1(y_1 - y_2) + \tau_3(y_1 - y_2)^3 - \Theta_{e1}V_{e1} - \theta_1\dot{y}_2 = F_{g1}, \tag{9a}$$

$$\ddot{y}_2 + \omega_2 y_2 + 2\omega_2\zeta_2\dot{y}_2 - \tau_1(y_1 - y_2) - \tau_3(y_1 - y_2)^3 - \Theta_{e2}V_{e2} - \theta_2\dot{y}_1 = F_{g2}, \tag{9b}$$

$$\dot{V}_1 + \eta_1 V_1 + \chi_1\dot{y}_1 = 0, \tag{9c}$$

$$\dot{V}_2 + \eta_2 V_2 + \chi_2\dot{y}_2 = 0, \tag{9d}$$

where the definitions of the normalized parameters in Eqs. (9) are listed in Table 1. The set of governing equations given in Eq. (9) indicates that the two primary and secondary oscillators are mechanically coupled to each other through a nonlinear magnetic force. Additionally, the oscillating aerodynamic wake force generated by the adjacent bluff body during oscillation is considered to avoid the loss of generality of the mathematical modeling although it has a tiny disturbance to the dynamic behaviors of bluff body compared to the magnetic force. It should be noted that the oscillating wake force acting to the bluff bodies is not equal due to the unilaterality of the incoming wind flow. Accordingly, an order selection considering the wake force scale should be conducted in finding analytical solution using perturbation method.

Table 1 Normalized parameters used in the governing equations, where $i = 1, 2$ denotes the primary and secondary oscillators, respectively.

Definition	Parameters
Undamped natural frequencies	$\omega_i = \sqrt{k_i / m_i}$
Damping ratios	$\zeta_i = c_i / \left(2\sqrt{m_i k_i}\right)$
Mass normalized electromechanical coupling coefficients	$\Theta_{ei} = \theta_{ei} / m_i$
Normalized wake coupling coefficients	$\tilde{\theta}_i^w = \theta_i^w / m_i$
Normalized magnetic force coefficients for primary oscillator	$\tau_1 = \mathrm{T}_1 / m_1, \tau_3 = \mathrm{T}_3 / m_1$
Normalized magnetic force coefficients for secondary oscillator	$\tilde{\tau}_1 = \mathrm{T}_1 / m_2, \tilde{\tau}_3 = \mathrm{T}_3 / m_2$
Capacitance normalized electromechanical coupling coefficients	$\tilde{\chi}_i = \theta_{ei} / C_{pi}$
Equivalent impedances	$\eta_i = 1 / R_{Li} C_{pi}$

2.3 Analytical solutions based on method of multiple scale

In an attempt to understand the nonlinear dynamic behaviors of the present system, especially the internal resonance between the individual oscillator, the perturbation method of multiple scale is utilized to obtain the approximate analytical solutions for Eq. (9). The time dependence can be expanded into two time scales in the form $T_0 = t$ (fast time scale) and $T_1 = \varepsilon t$ (slow time scale), respectively, where ε is a scaling parameter. The new time derivatives with respect to t can be expressed as:

$$\frac{\mathrm{d}}{\mathrm{d}t} = D_0 + \varepsilon D_1 + O\left(\varepsilon^2\right), \frac{\mathrm{d}^2}{\mathrm{d}t^2} = D_0^2 + 2\varepsilon D_0 D_1 + O\left(\varepsilon^2\right), \tag{10}$$

where $D_n = \dfrac{\partial}{\partial T_n}$ and $O\left(\varepsilon^2\right)$ denotes the terms higher than the second power of ε. The asymptotic

series solutions are expanded up to the first order, such that

$$
\begin{aligned}
y_1(T_0,T_1) &= \varepsilon^0 (y_1)_0 (T_0,T_1) + \varepsilon (y_1)_1 (T_0,T_1), \\
y_2(T_0,T_1) &= \varepsilon^0 (y_2)_0 (T_0,T_1) + \varepsilon (y_2)_1 (T_0,T_1), \\
v_1(T_0,T_1) &= \varepsilon^0 (v_1)_0 (T_0,T_1) + \varepsilon (v_1)_1 (T_0,T_1), \\
v_2(T_0,T_1) &= \varepsilon^0 (v_2)_0 (T_0,T_1) + \varepsilon (v_2)_1 (T_0,T_1),
\end{aligned}
\tag{11}
$$

where the symbols of $(\ )_0$ and $(\ )_1$ represent the ε^0 and ε^1 order solution for the dynamic responses of the primary and secondary oscillators. The oscillators in the present system are assumed to be weakly coupled by the external magnetic force and oscillating wake force. An ordering for the terms in Eq. (9) can be determined by scaling the viscous damping, magnetic coupling, electromechanical coupling, and aerodynamic force in the same order. In other words, the scaled relevant coefficients or terms can be expressed as

$$
\begin{aligned}
&\zeta_1 = \varepsilon\zeta_1,\ \zeta_2 = \varepsilon\zeta_2,\ \tau_1 = \varepsilon\tau_1,\ \tau_3 = \varepsilon\tau_3,\ \tilde{\tau}_1 = \varepsilon\tilde{\tau}_1, \\
&\tilde{\tau}_3 = \varepsilon\tilde{\tau}_3,\ \tilde{\theta}_1 = \varepsilon\tilde{\theta}_1,\ \tilde{\theta}_2 = \varepsilon^2\tilde{\theta}_2,\ \tilde{F}_{g1} = \varepsilon\tilde{F}_{g1},\ \tilde{F}_{g2} = \varepsilon\tilde{F}_{g2}.
\end{aligned}
\tag{12}
$$

It should be noted that the oscillating wake coupling coefficient generated by the secondary oscillator is defined to higher order of ε^2 considering the fact that the effect of the wake generated from the secondary oscillator to the primary bluff body is much weaker than that from the primary oscillator to the secondary oscillator generated. Substituting the scaled terms into Eq. (10) and expanding the governing equations in terms of Eq. (10) and (12), we can obtain the ordered equations after collecting the coefficients of ε^0 and ε^1, which yields the following results:

ε^0 order equations:

$$\frac{\partial^2}{\partial T_0^2}\left(y_1\right)_0+\omega_1^2\left(y_1\right)_0=0\,, \tag{13}$$

$$\frac{\partial^2}{\partial T_0^2}\left(y_2\right)_0+\omega_2^2\left(y_2\right)_0=0\,, \tag{14}$$

$$c_p\frac{\partial}{\partial T_0}\left(v_1\right)_0+\theta_e\frac{\partial}{\partial T_0}\left(y_1\right)_0+\frac{1}{R_{L1}}\left(v_1\right)_0=0\,, \tag{15}$$

$$c_p\frac{\partial}{\partial T_0}\left(v_2\right)_0+c_p\theta_e\frac{\partial}{\partial T_0}\left(y_2\right)_0+\frac{1}{R_{L2}}\left(v_2\right)_0=0\,. \tag{16}$$

ε^1 order equations:

$$\begin{aligned}\frac{\partial^2}{\partial T_0^2}\left(y_1\right)_1+\omega_1^2\left(y_1\right)_1&=-2\zeta_1\omega_1\frac{\partial}{\partial T_0}\left(y_1\right)_0+3\tau_3\left(y_1\right)_0{}^2\left(y_2\right)_0-3\tau_3\left(y_1\right)_0\left(y_2\right)_0{}^2-2\frac{\partial^2}{\partial T_0\partial T_1}\left(y_1\right)_0\\&+n_1U_1\,\mathrm{A}_{11}\frac{\partial}{\partial T_0}\left(y_1\right)_0+\frac{n_1\,\mathrm{A}_{13}}{U_1}\left(\frac{\partial}{\partial T_0}\left(y_1\right)_0\right)^3-\tau_1\left(y_1\right)_0+\tau_1\left(y_2\right)_0-\tau_3\left(y_1\right)_0{}^3+\tau_3\left(y_2\right)_0{}^3+\chi_1\left(v_1\right)_0\end{aligned}\,, \tag{17}$$

$$\begin{aligned}\frac{\partial^2}{\partial T_0^2}\left(y_2\right)_1+\omega_2^2\left(y_2\right)_1&=-2\zeta_2\omega_2\frac{\partial}{\partial T_0}\left(y_2\right)_0-3\tau_3\left(y_1\right)_0{}^2\left(y_2\right)_0+3\tau_3\left(y_1\right)_0\left(y_2\right)_0{}^2-2\frac{\partial^2}{\partial T_0\partial T_1}\left(y_2\right)_0\\&+n_2U_2\,\mathrm{A}_{21}\frac{\partial}{\partial T_0}\left(y_2\right)_0+\frac{n_2\,\mathrm{A}_{23}}{U_2}\left(\frac{\partial}{\partial T_0}\left(y_2\right)_0\right)^3-\tau_3\left(y_2\right)_0{}^3+\chi_2\left(v_2\right)_0+\theta_1\frac{\partial}{\partial T_0}\left(y_1\right)_0+\tau_1\left(y_1\right)_0-\tau_1\left(y_2\right)_0+\tau_3\left(y_1\right)_0{}^3\end{aligned}\,, \tag{18}$$

$$c_p\frac{\partial}{\partial T_0}\left(v_1\right)_1+\theta_e\frac{\partial}{\partial T_0}\left(y_1\right)_1+\frac{1}{R_{L1}}\left(v_1\right)_1=-c_p\frac{\partial}{\partial T_1}\left(v_1\right)_0-\theta_e\frac{\partial}{\partial T_1}\left(y_1\right)_0\,, \tag{19}$$

$$c_p\frac{\partial}{\partial T_0}\left(v_2\right)_1+c_p\theta_e\frac{\partial}{\partial T_0}\left(y_2\right)_1+\frac{1}{R_{L2}}\left(v_2\right)_1=-c_p\frac{\partial}{\partial T_1}\left(v_2\right)_0-c_p\theta_e\frac{\partial}{\partial T_1}\left(y_2\right)_0\,. \tag{20}$$

The solutions of the zeroth-order Eqs. (13)-(16) can be written as:

$$\left(y_1\right)_0=A_1\left(T_1\right)\mathrm{e}^{i\omega_1T_0}+cc\,, \tag{21}$$

$$\left(y_2\right)_0 = B_1\left(T_1\right)\mathrm{e}^{i\omega_2 T_0} + cc\,, \tag{22}$$

$$\left(v_1\right)_1 = -\frac{i\theta_e\omega_1 A_1\left(T_1\right)R_{L1}\mathrm{e}^{\omega_1 T_0 i}}{iR_{L1}c_p\omega_1 + 1} + \frac{i\theta_e\omega_1\overline{A_1}\left(T_1\right)R_{L1}}{\left(1\text{-}iR_{L1}c_p\omega_1\right)\mathrm{e}^{\omega_1 T_0 i}} + E_1(T_1)\mathrm{e}^{-\frac{T_0}{R_{L1}c_p}}\,, \tag{23}$$

$$\left(v_2\right)_1 = -\frac{i\theta_e\omega_2 B_1\left(T_1\right)R_{L2}\mathrm{e}^{\omega_2 T_0 i}}{iR_{L2}c_p\omega_2 + 1} + \frac{i\theta_e\omega_2\overline{B_1}\left(T_1\right)R_{L2}}{\left(1\text{-}iR_{L2}c_p\omega_2\right)\mathrm{e}^{\omega_2 T_0 i}} + E_2(T_1)\mathrm{e}^{-\frac{T_0}{R_{L2}c_p}}\,. \tag{24}$$

where cc denotes the complex conjugate of the preceding term. A_1 and B_1 denote the unknown complex-valued functions for primary and secondary oscillators, respectively. The over-bar denotes the complex conjugate. Substituting the zeroth-order solutions into the right hand side of the first order equations (17-20) and expanding the equations, it can be observed that frequency modes with frequency ratio of 1:1 are coupled via the oscillating wake force and the linear terms of magnetic force. Additionally, it also can be observed that the frequency modes with frequency ratio of 1:3 are coupled via cubic nonlinearities of the magnetic force. In this study, the 1:1 internal resonance plays a decisive role in the improvement of dynamic behaviors and the output performance for the present system referring to the results of a preliminary numerical analysis. After eliminating the undesired non-secular terms and collecting coefficients of harmonics, it can be obtained as follows:

$$\frac{\partial^2}{\partial T_0^2}\left(y_1\right)_1 + \omega_1^2\left(y_1\right)_1 = Q_1 e^{i\omega_1 T_0} + Q_2 e^{i\omega_2 T_0} + cc + NST\text{ , with} \tag{25}$$

$$Q_1 = \frac{3in_1 A_{13}A_1\left(T_1\right)^2\omega_1^3\overline{A}_1\left(T_1\right)}{U_1} - \frac{i\Theta_{e1}\theta_e\omega_1 A_1\left(T_1\right)R_{L1}}{iR_{L1}c_p\omega_1 + 1} - \tau_1 A_1\left(T_1\right) - 3\tau_3\overline{A}_1\left(T_1\right)A_1\left(T_1\right)^2\,,$$
$$-2i\left(\frac{\mathrm{d}}{\mathrm{dT_1}}A_1\left(T_1\right)\right)\omega_1 + in_1 U_1 A_{11}A_1\left(T_1\right)\omega_1 - 6\tau_3 A_1\left(T_1\right)\overline{B}_1\left(T_1\right)B_1\left(T_1\right) - 2i\zeta_1\omega_1^2 A_1\left(T_1\right)$$

$$Q_2 = 6\tau_3\overline{A_1}\left(T_1\right)A_1\left(T_1\right)B_1\left(T_1\right) + 3\tau_3\overline{B}_1\left(T_1\right)B_1\left(T_1\right)^2 + \tau_1 B_1\left(T_1\right).$$

$$\frac{\partial^2}{\partial T_0^2}\left(y_2\right)_1+\omega_2^2\left(y_2\right)_1=Q_3\mathrm{e}^{\omega_1 T_0 i}+Q_4\mathrm{e}^{i\omega_2 T_0}+cc+NST\text{ , with} \tag{26}$$

$$Q_3=3\tau_3\overline{A_1}\left(T_1\right)\left(A_1\left(T_1\right)\right)^2+6\tau_3 A_1\left(T_1\right)\overline{B_1}\left(T_1\right)B_1\left(T_1\right)+i\Theta_w A_1\left(T_1\right)\omega_1+\tau_1 A_1\left(T_1\right),$$

$$\begin{aligned}Q_4=&\,3\frac{in_2A_{23}\left(B_1\left(T_1\right)\right)^2\omega_2{}^3\overline{B_1}\left(T_1\right)}{U_2}-6\tau_3\overline{A_1}\left(T_1\right)A_1\left(T_1\right)B_1\left(T_1\right)-2i\zeta_2\omega_2{}^2B_1\left(T_1\right)-2i\left(\frac{\mathrm{d}}{\mathrm{d}T_1}B_1\left(T_1\right)\right)\omega_2\\&-3\tau_3\overline{B_1}\left(T_1\right)\left(B_1\left(T_1\right)\right)^2-\frac{i\Theta_{e2}\theta_e\omega_2B_1\left(T_1\right)c_pR_{L2}}{iR_{L2}c_p\omega_2+1}+in_2U_2A_{21}B_1\left(T_1\right)\omega_2-\tau_1B_1\left(T_1\right)\end{aligned}.$$

where NST stands for the terms that do not produce secular terms. Then, it is necessary to introduce the 1:1 internal resonance condition as

$$\omega_2=\sigma\varepsilon+\omega_1,\ \omega_1=-\sigma\varepsilon+\omega_2\,, \tag{27}$$

where σ is the internal resonance detuning parameter, which represents the closeness of the two natural frequencies of the primary and secondary oscillators. Substituting ω_2 and ω_1 in Eq. (27) into Eqs. (25)-(26) and after a mathematical manipulation, the simplified equations can be expressed as

$$\frac{\partial^2}{\partial T_0^2}\left(y_1\right)_1+\omega_1^2\left(y_1\right)_1=\left(Q_1+Q_2e^{i\sigma T_1}\right)e^{i\omega_1T_0}+cc+NST\,, \tag{28}$$

$$\frac{\partial^2}{\partial T_0^2}\left(y_2\right)_1+\omega_2^2\left(y_2\right)_1=\left(Q_3+Q_4e^{-i\sigma T_1}\right)e^{i\omega_2T_0}+cc+NST\,. \tag{29}$$

Eliminating the terms that lead to secular terms in the above equations, and expressing the complex-valued function in the polar form

$$A_1\left(T_1\right)=\frac{a\left(T_1\right)\mathrm{e}^{i\beta_1(T_1)}}{2}, B_1\left(T_1\right)=\frac{b\left(T_1\right)\mathrm{e}^{i\beta_2(T_1)}}{2}, \tag{30}$$

where a and b represent the unknown amplitude for the primary and secondary oscillators; β_1 and β_2 represent the phase of the corresponding dynamic responses. Next, separating the real and imaginary parts in Eqs. (28)-(29) yields the modulation equations as

$$\frac{\mathrm{d}a}{\mathrm{d}T_1}=\frac{U_1 b\sin(\Upsilon)\left(6\tau_3 a^2+3\tau_3 b^2+4\tau_1\right)+a\left(4U_1^2 n_1 \mathrm{A}_{11}\omega_1-8U_1\omega_1^2\zeta_1-4U_1E_{12}\right)+3a^3 n_1\mathrm{A}_{13}\omega_1^3}{8U_1\omega_1}, \tag{31}$$

$$\frac{\mathrm{d}\beta_1}{\mathrm{d}T_1}=\frac{a\left(4E_{11}+3\tau_3 a^2+6\tau_3 b^2+4\tau_1\right)-\left(6\tau_3 a^2 b+3\tau_3 b^3+4\tau_1 b\right)\cos(\Upsilon)}{8\omega_1 a}, \tag{32}$$

$$\frac{\mathrm{d}b}{\mathrm{d}T_1}=\frac{-aU_2\sin(\Upsilon)\left(3\tau_3 a^2+6\tau_3 b^2+4\tau_1\right)+4U_2 a\omega_1\Theta_w\cos(\Upsilon)+3b^3\omega_2^3 n_2\mathrm{A}_{23}+\left(4\omega_2 U_2 n_2\mathrm{A}_{21}-8\zeta_2\omega_2^2-4E_{22}\right)U_2 b}{8\omega_2 U_2}, \tag{33}$$

$$\frac{\mathrm{d}\beta_2}{\mathrm{d}T_1}=\frac{\left(-3\tau_3 a^3-6\tau_3 ab^2-4\tau_1 a\right)\cos(\Upsilon)-4a\omega_1\Theta_w\sin(\Upsilon)-b\left(-6\tau_3 a^2-3\tau_3 b^2+4E_{21}-4\tau_1\right)}{8\omega_2 b}, \text{ with} \tag{34}$$

$$\gamma=\sigma T_1+\beta_2-\beta_1, E_{11}=\frac{\Theta_{e1}\theta_e c_p\omega_1{}^2R_{L1}^2}{R_{L1}{}^2c_p{}^2\omega_1{}^2+1}\quad E_{12}=\frac{\Theta_{e1}\theta_e\omega_1 R_{L1}}{R_{L1}{}^2c_p{}^2\omega_1{}^2+1},$$

$$E_{21}=\frac{\Theta_{e2}\theta_e c_p\omega_2{}^2R_{L2}^2}{R_{L2}{}^2c_p{}^2\omega_2{}^2+1}\quad E_{22}=\frac{\Theta_{e2}\theta_e\omega_2 R_{L2}}{R_{L2}{}^2c_p{}^2\omega_2{}^2+1}.$$

The time derivatives of β_1 and β_2 in Eq. (32) and (34) can be vanished in terms of the relationship of $\gamma'=\sigma+\beta_2'-\beta_1'$, where the primer means the time derivation of T_1, and thus the modulation equations with 4-dimensional phase space (a, b, β_1, β_2) can be reduced to a 3-dimensional phase space (a, b, γ). Additionally, the steady-state responses can be determined by setting the time derivatives in the

modulation equations equal to zero. The resulted equations are a set of transcendental equations which are difficult to be solved by an analytical method, however, it is fairly straightforward to be solved numerically for semi-analytical solutions. Subsequently, we can obtain the output voltage generated by the piezoelectric element using Eqs. (23) and (24), where homogeneous and non-homogeneous solutions are contained in them. It is known that the homogeneous solutions would converge to zero on account of the electric energy dissipation in the external resistor along the time. Consequently, we can find the output voltage amplitude through the non-homogeneous terms, and the resultants can be expressed with a function of the amplitude of the corresponding oscillators as

$$V_1 = \frac{\theta_e \omega_1 R_{L1}}{\sqrt{R_{L1}^2 c_p^2 \omega_1^2 + 1}} |a|, \; V_2 = \frac{\theta_e \omega_2 R_{L2}}{\sqrt{R_{L2}^2 c_p^2 \omega_2^2 + 1}} |b|. \tag{35}$$

Subsequently, the output power can be described as

$$P_1 = \frac{\theta_e^2 \omega_1^2 R_{L1}}{R_{L1}^2 c_p^2 \omega_1^2 + 1} |a|^2, \; P_2 = \frac{\theta_e^2 \omega_2^2 R_{L2}}{R_{L2}^2 c_p^2 \omega_2^2 + 1} |b|^2. \tag{36}$$

According to the expressions of output voltage and power, we can compare the energy harvesting performance between the internal resonance case and non-internal resonance case.

3 Oscillating wake induced internal resonance

Table 2 Physical parameters used in the proposed system.

Description	Symbol	Value
Mass of bluff bodies	m_1 , m_2	0.015 kg, 0.01 kg
Characteristic dimension of the bluff bodies	D	30 mm
Height of the bluff bodies	H_1 , H_2	100 mm, 80 mm
Damping constants	c_1 , c_2	0.0021 Ns/m, 0.0015 Ns/m
Stiffness of spring	k_1	236.86 N/m
Electromechanical coupling coefficients	$\theta_{e1} = \theta_{e2} = \theta_e$	1.1×10^{-4} N/V
Capacitance of the piezoelectric patches	$C_{p1} = C_{p2} = C_p$	90 nF
1st and 3rd order aerodynamic coefficients [38]	$A_{11} = A_{21}, A_{13} = A_{23}$	2.3,-18.4
Air density	ρ_a	1.225 kg/m^3
Magnitudes of magnetization	$\bar{m}_1 = \bar{m}_2$	0.295×10^6 A/m
Volumes of magnets	$\bar{v}_1 = \bar{v}_2$	40π mm^3
Vacuum permeability	μ_0	$4\pi\times10^{-7}$ H/m

In this section, we first investigated the electric characteristics of the external circuit and some fundamental aerodynamic features as a preliminary investigation for the further examination of coupled dynamic behaviors. Additionally, the oscillating wake generated from the primary bluff body has an effect to the dynamic behaviors secondary bluff body. To validate the proposed analytical model and give a comprehensive understanding of oscillating wake coupled system, we examine the dynamic behaviors considering the pure oscillating wake coupling effect by assuming the magnet gap distance to be infinite. Subsequently, some bifurcation analyses are carried out to clarify the inherent characteristics

of the internal resonance. The relevant parameters and the corresponding values used in this study are listed in Table 2.

3.1 Effect of the external resistance

In a wind energy harvesting system, the critical wind speed is one of the most important factors to evaluate the output performance. Here, we first investigate and clarify the influence of external load to the critical wind speed in terms of the secular equations. The energy harvesting system would loss stability when the linear mechanical damping changes to be negative. Nevertheless, the resultant damping term is determined by the combined effect of the mechanical damping and the electric damping in an electromechanical coupled system. Based on the simplified secular equations, the derived damping coefficient can be expressed as

$$U_i \mathrm{A}_{21}\omega_i n_i - 2\zeta_i\omega_i^2 - E_{i2} \geq 0 . \tag{37}$$

The critical wind speed can thus be expressed as

$$U_{cri} = \frac{2\zeta_i\omega_i + \dfrac{\Theta_{ei}\theta_e R_{Li}}{R_{Li}^2 c_p^2 \omega_i^2 + 1}}{n_i A_{11}} . \tag{38}$$

According to the expression of critical wind speed, we can investigate the relationship between the external resistance and the critical wind speed. As shown in Fig. 2, the critical wind speed changes to be higher as the external resistance increases and then decline with the further increase of the external resistance, which matches the results in [39]. The up and down phenomenon of critical wind speed

versus external resistance is resulted from the electromechanical damping terms of E_{i2}, which causes an maximum value damping at the resistance value of 0.176 MΩ for the primary oscillator. The resistance value is also regarded as an optimal one to obtain a maximum output power in the external circuit. As shown in Fig. 2(a), the electromechanical coupling strength also shows a significant influence to the critical wind speed. It can be observed that the strong coupling effect between electric domain and mechanical domain would result in an increase of critical wind speed. On the other hand, the detuning parameter σ describes the difference between the natural frequencies of the primary and secondary oscillators, which causes the change of the secondary natural frequency as shown in Fig. 2(b). It further indicates the fact that the increase of natural frequency is able to pull down the critical wind speed.

In a general energy harvesting system, impedance matching between mechanical and electric system is essential to obtain a maximum output power. Mechanical energy would be dissipated during energy harvesting operation due to the fact that the mechanical energy is transformed into electric energy. However, the increase of electric damping results in a dramatic decrease in the dynamic response of oscillator as shown in Fig. 3, especially in the low wind speed range. This result gives a pertinent interpretation for the fact that the critical wind speed is postponed as the external resistance near to the optimal value as shown in Fig. 2. For a consistent evaluation of the effect of internal resonance and other key parameters, the external resistance is treated to be infinite, in other words, an open circuit in the next section.

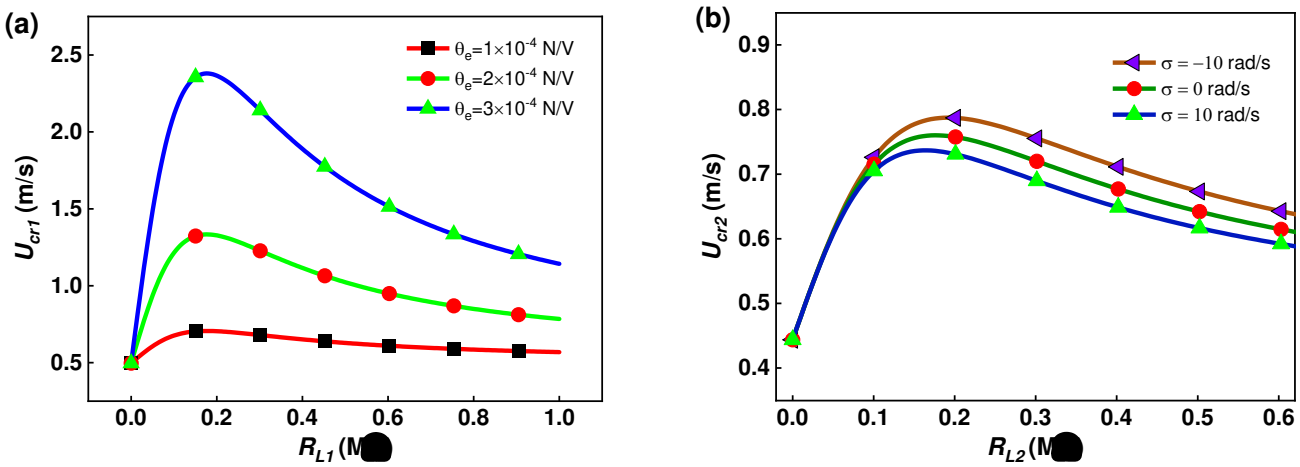

Fig. 2 Variation of critical wind speed versus external resistance with different (a) electromechanical coupling coefficients, (b) detuning parameters.

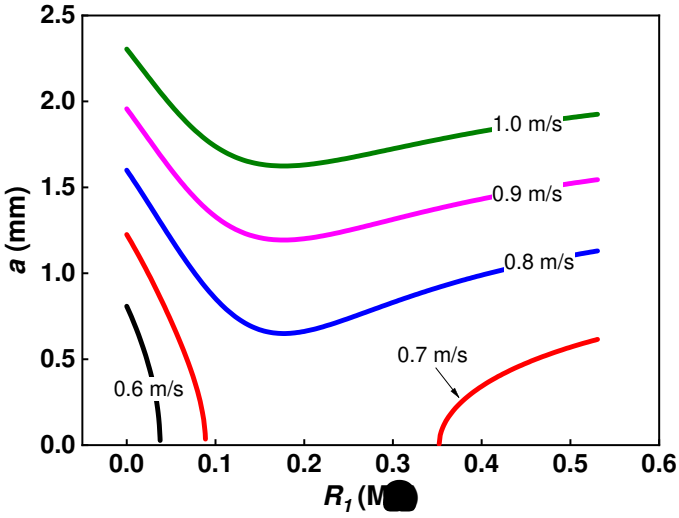

Fig. 3 Electric damping effects to the amplitude of the primary oscillator under different wind speeds.

3.2 Parametric analyses under wake effect

In this subsection, we investigated the dynamic responses of both oscillators under no magnetic force coupling by setting the distance between two magnets infinity. The oscillating wake generated by

the primary bluff body periodically acts on the secondary bluff body, however, it is not easy to inversely affect that of the primary bluff body. This phenomenon is analytically and numerically investigated, and the results are shown in Fig. 4(a). In this numerical calculation, we adopted a means of wind speed sweeping to illustrate the evolution of dynamic behavior with time. Through comparing the numerical results to the analytical ones, a good matching can be seen in a wind speed range from 0 m/s to 10 m/s.

The strength of the incoming wind exerted on the secondary bluff body tends to be weaker due to the wind flow obstruction of the primary bluff body configured in front of the secondary bluff body, in other words, the actual wind speed loaded to the secondary bluff body is smaller than that to the primary one. This fact necessitates a function relationship between the wind speeds of U_1 and U_2. We assume that U_2 is linearly related to U_1 and expressed as $U_2 = \eta U_1$. Here, η is a wind speed proportional constant to quantitatively express the reduction of wind speed, which always smaller than one. Subsequently, we analytically investigated the amplitude responses of the secondary bluff body versus wind speed under different η with Θ_w =0 Ns/m and σ =0 rad/s as shown in Fig.4 (b). It can be seen that the amplitudes of the bluff body increase along the axis of the wind speed for all the various η cases. However, the critical wind speed moves to the higher range as η decreases. The subplot in Fig.4 (b) shows the variation of dimensionless critical wind speed $\bar{U}_{cr}$ (U_{cr}/U_0) over the wind speed proportional constant η, where U_0 denotes the critical wind speed when η is zero. It further shows that $\bar{U}_{cr}$ is much sensitive to the variation of η at low range of η, which demonstrated a dramatical increase as η close to zero.

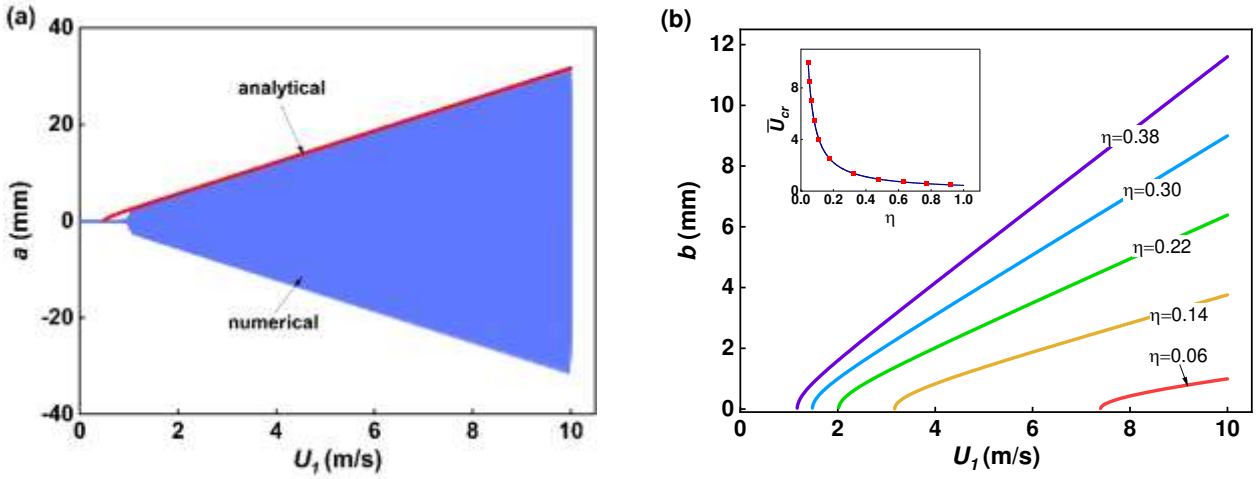

Fig. 4 (a) Results comparisons Electric damping effects to the amplitude of the primary oscillator under different wind speeds with $\Theta_w = 0$ Ns/m and $\sigma = 0$ rad/s.

A natural difference of the dynamic responses happens in the secondary bluff body when the wake coupling effect is accounted for in the dynamical analysis. Response bifurcation and multiple solution phenomenon start to appear when Θ_w is given a small value of 0.002 Ns/m as shown in Fig. 5. Here, two stable branches and one unstable branch can be determined through the stability evaluation based on the eigenvalues of the Jacobian matrix of the right-hand sides of Eqs. (31) – (34) as stated in [40]. The cross point between the bifurcation curve and the dynamic response curve is defined as the saddle node. It can be clearly observed that the critical wind speed is pulled down to the lower wind range referring to that case without consideration of wake oscillation. In addition, it is also observed that the saddle node can be significantly reduced from 9.2 m/s to 3.8 m/s as η increases from 0.08 to 0.16, and the second stable branch tends to be close to the first stable branch as η increases as illustrated in Fig. 5 (a) and (b).

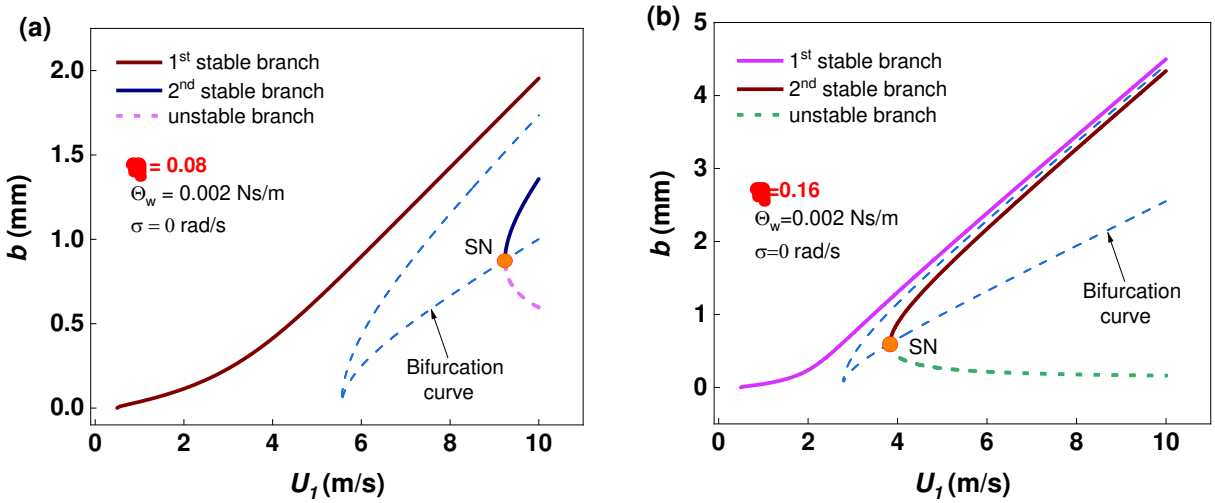

Fig. 5 Bifurcation graph of secondary bluff body response under (a) η =0.08 and (b) η =0.16 with Θ_w =0.020 Ns/m and σ =0 rad/s.

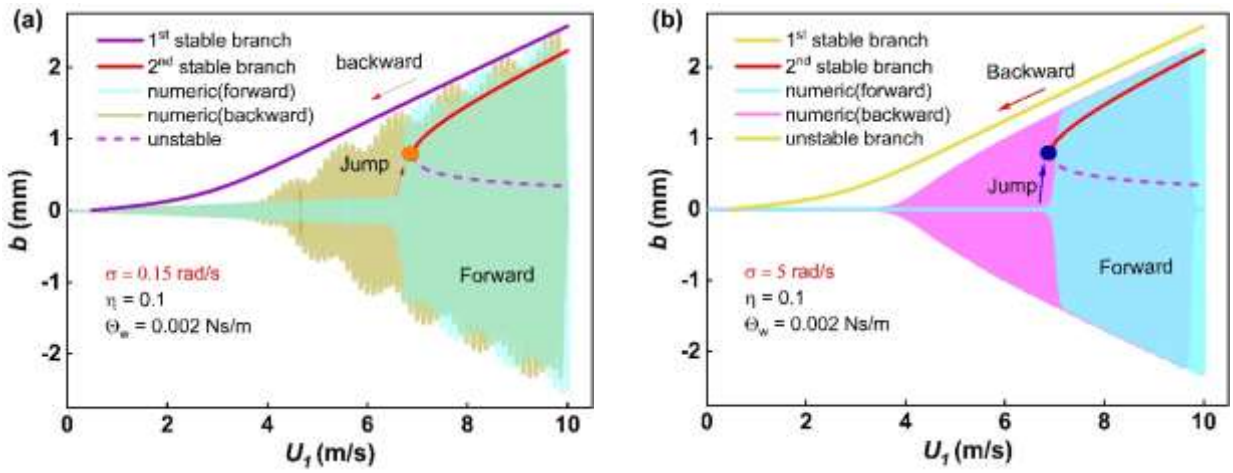

Fig. 6 comparisons between analytical prediction results and numerical results with forward and backward sweeping of wind speed under (a) σ =0.15 rad/s and (b) σ =5 rad/s with Θ_w =0.020 Ns/m and η =0.1.

The influence of detuning parameter σ to the dynamic response of the secondary bluff body is also investigated in the presence of oscillating wake coupling as shown in Fig. 6. The graphs depicted similar dynamic behaviors with the cases showed in Fig. 5, however, we can see that the variation of σ exhibits

few effects to the saddle node position, which is much different with the varying case of η. To further evaluate the analytical results, a series of numerical simulation have been conducted by sweeping the parameter with variation of time. A jump phenomenon occurs at the saddle node point when the wind speed increases from zero to higher wind speed range both in $\sigma = 0.15$ and $\sigma = 5$ cases as shown in Fig. 6 (a) and (b). It is worth noting that the maximum amplitude appears close to the first stable branch at a smaller σ and which tends to approach the second stable branch when a bigger σ is introduced. On the other hand, the amplitude responses decrease along the routine of the first stable branch when a wind speed decreases backward. From the above comparisons, a good matching between the analytical and numerical results are achieved, which further validates the proposed prediction model.

3.3 Perspective in saddle-node bifurcation

As previously mentioned, the saddle node point appears as we vary the associated parameters, the saddle node plays an important role in the dynamic response evaluation for a nonlinear coupled system. Accordingly, a systematical analysis for the overall bifurcation curve is necessary at the viewpoint of revealing the mechanism contained in the wake coupled oscillators. Response bifurcation usually happens at the positions where the derivative of the response to the varying parameter is zero. A 3-Dimensional graph for the amplitude of the secondary oscillator in terms of two varying parameters can be identified based on the resultant polynomial equation. It is expected that a surface fold phenomenon of the dynamic response would happen due to the non-linearity of the coupled parameter and aerodynamic force.

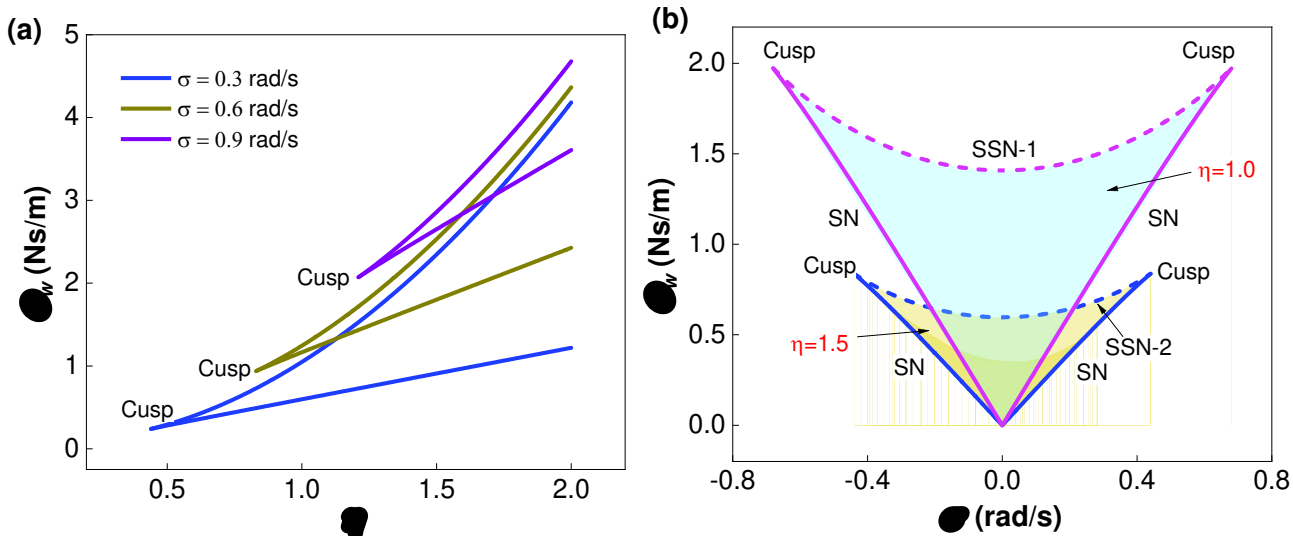

Fig. 7 Saddle node bifurcation of oscillating wake coupled nonlinear oscillator in (a) $\eta-\Theta_w$ plane and $\sigma-\Theta_w$ plan.

For a coherent exhibition of the saddle-node bifurcation curve, we reduce the polynomial equation including 3 varying parameters to that including 2 parameters by vanishing the amplitude of secondary oscillator using the original polynomial equation and its derivative with the amplitude of secondary oscillator. As shown in Fig. 7, a series of saddle-node bifurcation curves are generated in $\eta-\Theta_w$ and $\sigma-\Theta_w$ plane where the stable and unstable fixed points collide. Additionally, a cusp bifurcation occurs when two saddle-node bifurcation curves meet as shown in Fig. 7(a) and (b). The folds degenerate at these cusp point, that is, the frequency synchronization tends to be difficult when the varying parameter passing the cusp point. It shows that cusp point moves to higher values of η and Θ_w as σ increases as illustrated in Fig. 7(a). In Fig. 7(b), the shadow regions are bounded by the saddle node curves and saddle-node bifurcation curve for a saddle and a twice saddle cycles (SSN). There cusp points appear in each bounded region. We can see from this graph that the shadow region is symmetric with the axis of

σ =0, which indicates the bounded synchronization region is strongly dependent on the natural frequency difference of the two oscillators. Furthermore, η gives a significant influence to the area of the bounded regime, namely the increasing of η causes area expansion of the bounded regime.

4 Magnetically force induced internal resonance

The fundamental dynamic behaviors of the oscillators undergoing oscillating wake coupling have been parametrically investigated in the previous section without consideration of real physical conditions. In galloping-based energy harvesting, an asymmetric bluff body is usually adopted to generate the transverse aerodynamic force, which leads to vibration of oscillator as the system loses its stability. In the galloping phenomenon, the wake shed from the asymmetric bluff body is easy to be broken as wind flow is strongly separated for the edge of the bluff body, in which the wake intensity would be significantly reduced. As an alternative, we consider to utilize weak magnetic force effect to bring out the internal resonance for an improving energy harvesting performance. In this section, we concentrate on the clarification of synchronization mechanism and evaluation of the improving performance of the magnetically coupled wind energy harvester under internal resonance.

4.1 Synchronization analysis

To further validates the analytical solution in the magnetically coupled case, we compared the analytical predictions and numerical solutions by examining the effect of some key parameters on the dynamic responses of the primary and secondary oscillators. Herein, the numerical solutions were

obtained by sweeping the parameters with varying time. Fig. 8 shows the dynamic responses for each oscillator when the detuning parameter changes with fixed associated parameters, in which a very good matching between the analytical predictions and numerical solutions can be observed throughout the concerned range of detuning parameter. This graph shows that a slight amplitude decreasing of the primary oscillator (Fig. 8(a)) corresponding a significant amplitude increase of the secondary oscillator (Fig. 8(b)) as σ near to zero, where the 1:1 internal resonance happens. This phenomenon indicates an energy exchange happens between the two modes of oscillation during their oscillating. It is worth noting that not only stable solutions, but unstable branch of the secondary bluff body were observed in the analytical prediction as shown in Fig. 8(b). The unstable branch is strongly dependent on the wind speed proportional constant η, in other words, this unstable branch is directly induced by the wind flow applied to the bluff body.

In purpose of representing the dynamic strength distribution over time at various frequencies and examinating the frequency or amplitude synchronizing regime, spectrograms via fast Fourier transformation are adopted as shown in the second row of figure 8. It can be observed that a concentrated and consistent energy distribution of the primary oscillator is located near 20 Hz, and the similar phenomenon can be found in the spectrogram of the secondary oscillator even though there appears some energy distribution in other frequency regimes. This spectrogram indicates that the oscillating frequency of secondary oscillator is locked on that of the primary oscillator. However, secondary natural frequency varies by adjusting detuning parameter σ, which gives rise to some sub-

harmonic or super-harmonic responses in the secondary oscillators as shown in the spectrogram of secondary oscillator. Obviously, the energy distribution level is higher as σ closed to zero, which reflects that the advantages of using 1:1 internal resonance in improving energy conversion efficiency from wind energy to structural vibration energy, and further enhancing the wind energy harvesting performance.

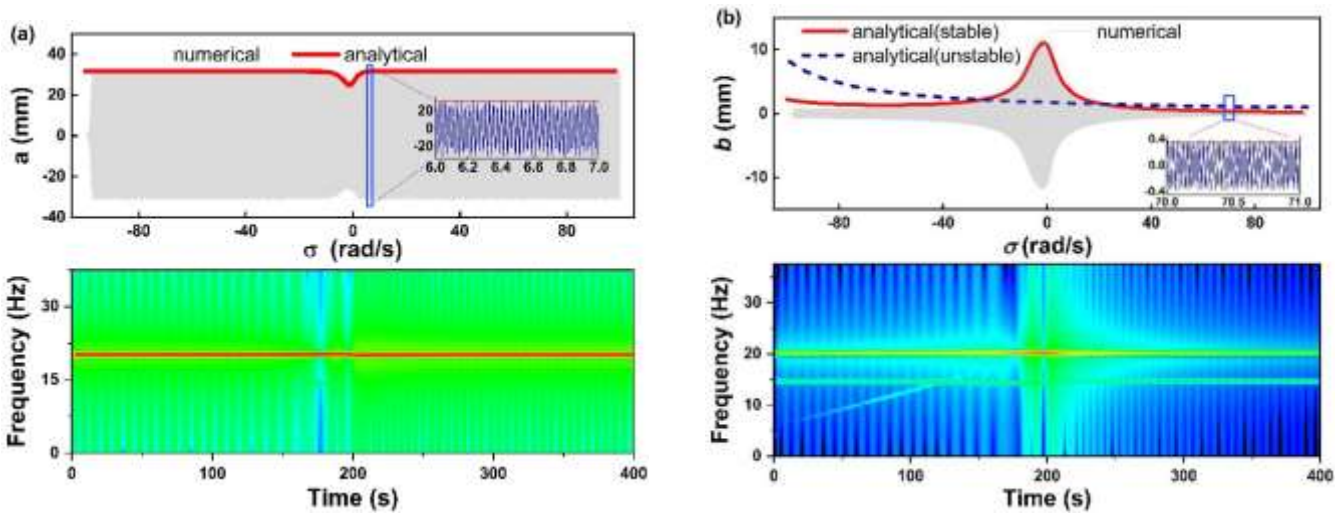

Fig. 8 Dynamic resonances comparisons between analytical results and numerical results versus varying of natural frequency differences and spectrogram for (a) primary oscillator, (b) secondary oscillator and the spectrograms for each oscillator at D_m = 20 mm $\Theta_w = 0.08$, U_1 = 10 m/s and $\eta = 0.08$.

As the wind speed proportional constant η increases to 0.16, the wind flow induced response curve changes from unstable branch to stable branch as shown Fig. 9 (b). In this case, the dynamic response of the secondary oscillator exhibits a combination of the two stable branches. It also shows that the secondary oscillator amplitude is enlarged as σ closed to zero owing to the frequency lock-in phenomenon as shown in the spectrogram of secondary oscillator. Comparing to the case with η =0.08,

the increase of the strength of the wind flow applied to the secondary oscillator promotes the occurrence of the galloping induced vibration, and further to be dominant response. It can be observed in the secondary spectrogram that the main energy concentration varies over time following the increasing of σ with time variation, which means the secondary oscillator oscillates with itself ascendant natural frequency. Subsequently, some slight changes in oscillating frequency of the primary oscillator happens when η increases to 0.16 as shown in the spectrogram of the primary oscillator.

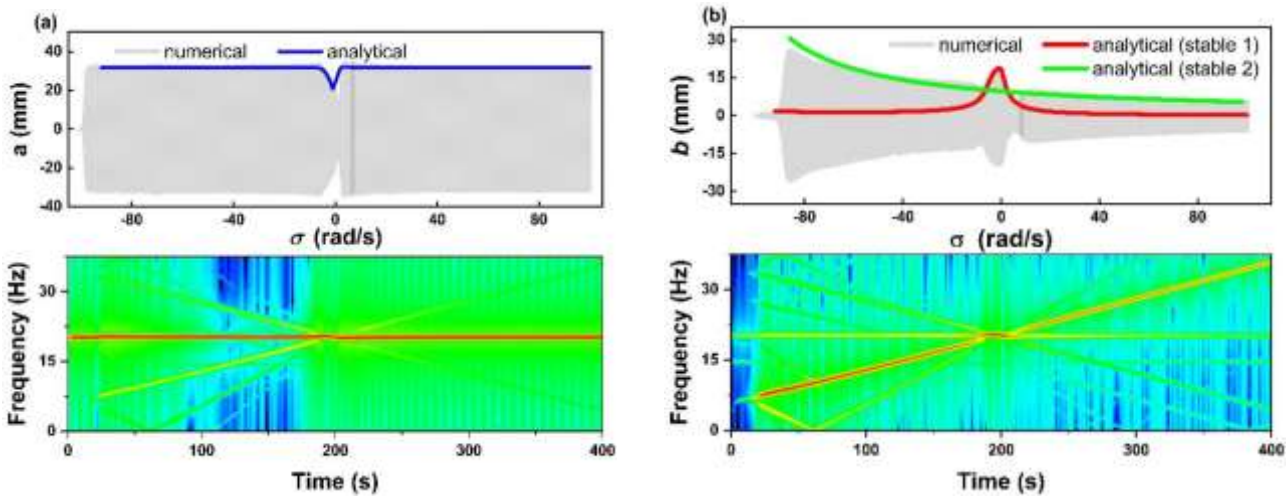

Fig. 9 Dynamic resonances comparisons between analytical results and numerical results versus varying of natural frequency differences and spectrogram analysis for (a) primary oscillator, (b) secondary oscillator and the spectrograms for each oscillator at D_m = 20 mm, Θ_w =0.08, U_1 =10 m/s at η =0.16.

As mentioned in the previous section, η plays an important role in dynamic response of the secondary oscillator. In a practical situation, η is usually a very small value due to the strength deduction of wind flow as experimentally investigated in [35]. Accordingly, it becomes necessary to improve the energy harvesting performance by using magnetic force induced synchronization phenomenon. However, a approximate magnetic force is essential for an induction of synchronization

because a strongly mode coupling will result in a structural binding phenomenon, which cause the 2-DOF system collapse to a 1-DOF system. On the other hand, an extremely weak coupling would cause invalidation of mode coupling, and thus make synchronization phenomenon hard to happen. In this study, we investigated the influence of magnet distance to the responses of both oscillators. Subsequently, we investigated the dynamic responses of both the oscillators with a small magnet distance for a strongly mechanical coupling, and the results are illustrated in Fig. 10. It can be observed that both of the primary and secondary oscillators are totally bounded to each other, and they have almost the same dynamic behaviors over the varying frequency range. Based on the prediction accuracy point, it can be found that the analytical prediction results showed in the Fig. 10(a) and (b) does not give an accurate amplitude matching with that of the numerical results. The difference between numerical results and analytical prediction happens because chaos phenomenon happens in this strongly coupled system as detuning parameter σ varies, and chaos itself is hard to be predicted. In the spectrogram of each oscillator in second row of Fig. 10, it can be identified that a frequency evolution happens over time, especially, the frequencies evolution is irregular and infinite in the chaos regions. The other regime except the chaos ones also shows a quasi-chaos state even though the dominant frequencies exhibit the same trend of gradual increasing for both of the oscillators.

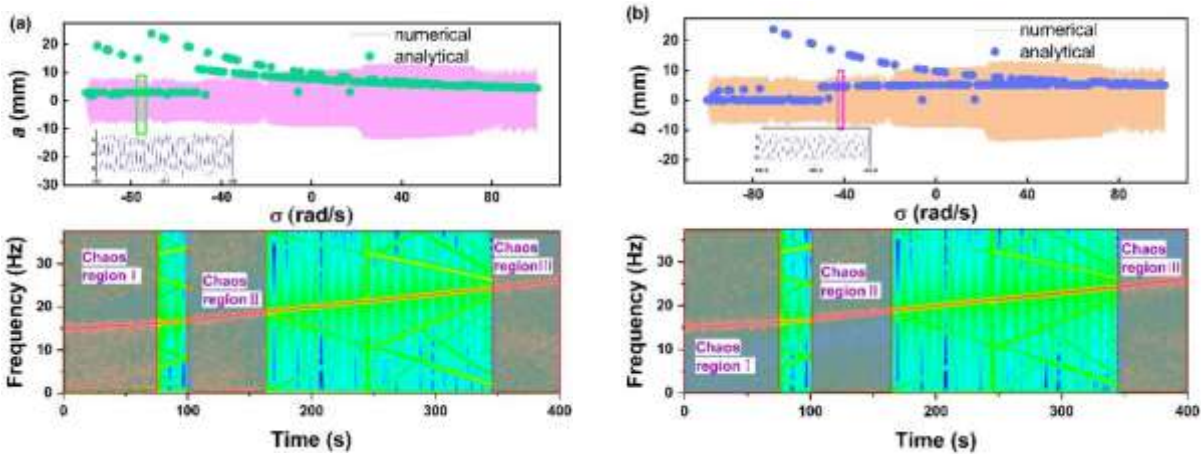

Fig. 10 Dynamic resonances comparisons between analytical results and numerical results versus varying of natural frequency differences for (a) primary oscillator, (b) secondary oscillator and the spectrograms for each oscillator at $\Theta_w = 0.08$, $U_1 = 10$ m/s, $\eta = 0.08$ at $D_m = 5$mm.

To further clarify the influence of the magnetic force strength to the system dynamic responses, we conducted an analytical investigation and compared the dynamic behaviors of the oscillators according to various magnet distances, and the results are shown in Fig. 11. It can be observed that the energy bounded phenomenon happens at the magnet distance of 20 mm, where an amplitude ascending of the primary bluff body corresponds an amplitude descending of the secondary oscillator. Additionally, in this case, the wind flow induced response exhibits unstable. As the magnet distance increases to 40 mm, the energy bounded effect tends to be recessive and a combined dynamic response happens. The wind flow induced response becomes dominant as the magnet distance further increases to 60 mm. In summary, an appropriate magnet distance is significant in improving the effect of energy transform between dynamic modes.

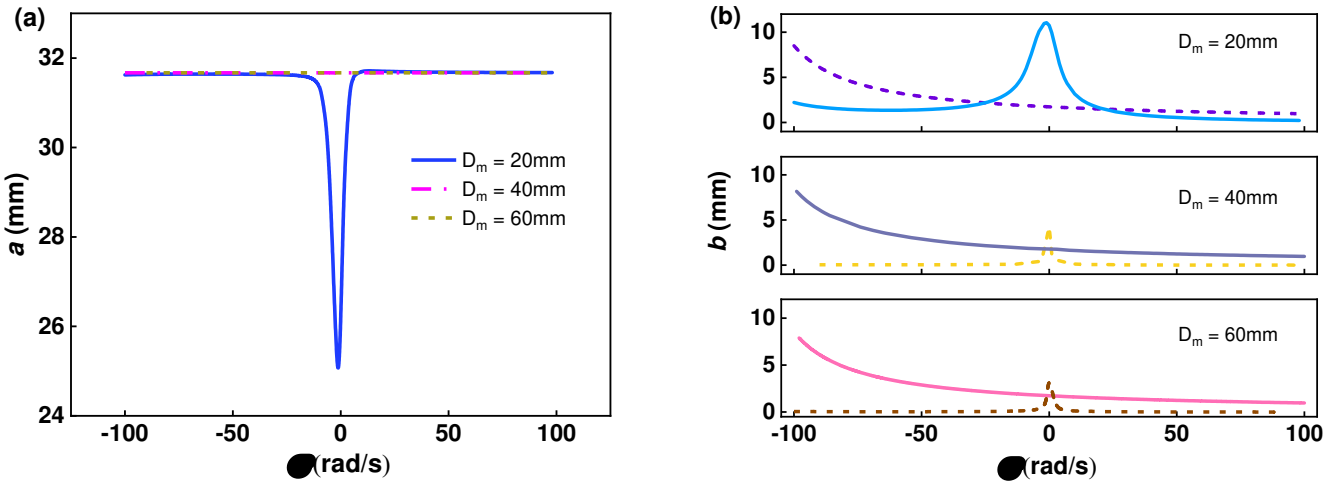

Fig. 11 Dynamic resonances comparisons versus varying of natural frequency differences for (a) primary oscillator, (b) secondary oscillator under different magnet distances of 20 mm, 40mm and 60 mm.

4.2 Performance evaluation

The 1:1 internal resonance is adopted for the mode synchronization between the oscillators, and thus the output performances are expected to be effectively improved. In this study, a maximum power based on an optimal resistance is assumed to evaluate the output performance.

The total RMS voltage are calculated to combine the output voltages from the primary and secondary oscillators according to Eq. (35) with an optimal resistance of 0.18 MΩ. Subsequently, the total maximum average power can be calculated according to Eq. (36). As shown in Fig. 12, the output voltage and average power undergoes a dramatic decrease when σ near zero (namely the difference between two natural frequency is closed to zero) at an extremely small magnet distance of 15 mm, because a collapse of degree freedom number happens when the coupling force exceeds a throttle value. It can be seen that total RMS voltage with the maximum value of about 60 V and average power of

0.021 W with two peaks happens near the position when σ is zero as the magnet distance increases to 20 mm. Subsequently, as we continually increase the magnet distance to 25 mm, two electric output peaks changes to one single peak near the position where σ equals zero as shown in Fig. 12.

In summary, a significant enhancement of both the total RMS voltage and average power can be achieved by exploiting of the nonlinear magnet force coupling. The 1:1 internal resonance of two oscillators leads to frequency synchronization as natural frequencies of two oscillators are closed to each other, and further promoting the output performance enhancement.

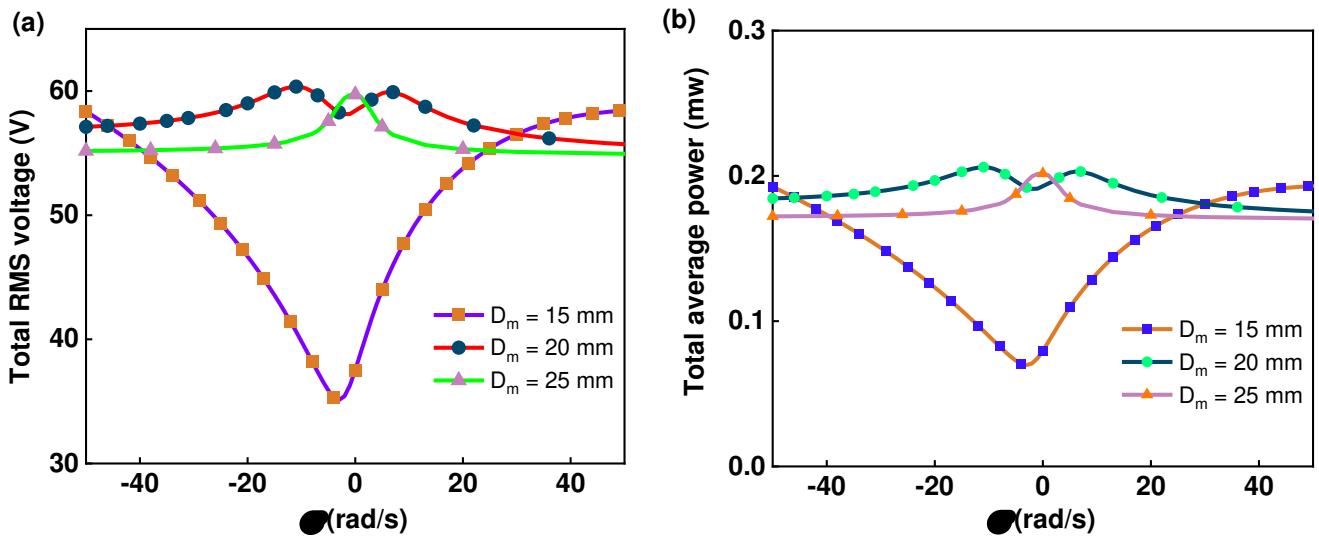

Fig. 12 (a) Total RMS voltages and (b) average powers against various σ under different magnet distance of 15 mm, 20 mm and 25 mm.

5 Conclusions

In this study, we proposed a technique of 1:1 internal resonance to improve the output performance in a magnetically coupled wind energy harvester with two tandem oscillators which are arranged along the wind flow direction. The proposed technique was numerical and analytically verified advantageous,

while a significant improvement of total RMS voltage and average power are readily achieved as the frequency synchronization happens when the two natural frequency equals to each other.

The magnetically coupled governing equations representing the transverse dynamics of the bluff bodies and electric circuitry are derived based on the extended Hamilton principle. The oscillating wake generated by the primary bluff body are considered in the proposed model to investigate the dynamic behaviors of both the oscillators. The approximate analytical solutions of the resulting model are determined using a perturbation technique: the method of multiple scales. After mathematical manipulation, a set of modulation equations are obtained to predict the overall static dynamic responses. The proportional wind flow constant η is newly defined in this study to describe the wind velocity reduction to the secondary bluff body. A series of parametric studies are carried out to obtain a comprehensive understanding of the relationships between the system dynamic behaviors and the parameters including wind velocity U_1, frequency detuning parameter σ and oscillating wake coefficient Θ_w with absence of magnetic force. The comparisons between the analytical prediction solutions and numerical results are also conducted, which exhibits a very good matching between them. Several saddle-node bifurcation analyses are conducted to reveal the nature of the system with $\eta-\Theta_w$ and $\sigma-\Theta_w$ plane. The cusp bifurcation and synchronization region are found out based on the bifurcation analyses.

The frequency synchronization under magnetic coupling can be triggered as the natural frequencies of the oscillators close to each other under a suitable magnet distance and verified both in analytical

prediction solutions and numerical results. The total RMS voltages and average power generated by both of the oscillators shows a significant improvement when the magnet distance larger than 15 mm which is benefit to promote the improvement of energy harvesting performance. This study provides an important guideline for the design of a magnetically coupled high-efficiency 2-DOF wind energy harvester using the 1:1 internal mode resonance. It is expected that the proposed method has a potential in designing compact and efficient wind energy harvesters and broad and practical industrial applications such as wireless sensor networks in the future.

Acknowledgments

This work was supported by the National Natural Science Foundation of China (5210051321) and Scientific Research foundation for Talented Scholars of Jiangsu University (5501730000).

Data availability statement

All data generated or analysed during this study are included in this published article (and its supplementary information files).

Conflict of Interest

The authors declare that they have no conflict of interest.

References

1. Zhang, L., Meng, B., Xia, Y., Deng, Z., Dai, H., Hagedorn, P., et al.: Galloping triboelectric nanogenerator for energy harvesting under low wind speed. Nano Energy. **70**, 104477 (2020) https://doi.org/10.1016/j.nanoen.2020.104477

2. Wang, G., Liao, W.-H., Zhao, Z., Tan, J., Cui, S., Wu, H., et al.: Nonlinear magnetic force and dynamic characteristics of a tri-stable piezoelectric energy harvester. Nonlinear Dynamics. **97**(4), 2371-97 (2019) https://doi.org/10.1007/s11071-019-05133-z
3. Maamer, B., Boughamoura, A., Fath El-Bab, A.M.R., Francis, L.A., Tounsi, F.: A review on design improvements and techniques for mechanical energy harvesting using piezoelectric and electromagnetic schemes. Energy Convers Manage. **199**, 111973 (2019) https://doi.org/10.1016/j.enconman.2019.111973
4. Dai, J., Tan, Y., Shen, X.: Investigation of energy output in mountain wind farm using multiple-units SCADA data. Appl Energy. **239**, 225-38 (2019) https://doi.org/10.1016/j.apenergy.2019.01.207
5. Kaplan, Y.A., Agalar, S., Bildircin, H.: General situation of wind energy source in Turkey and wind turbine technologies. International Journal of Renewable Energy Technology. **10**(1-2), 56-67 (2019) https://doi.org/10.1504/IJRET.2019.097004
6. Sun, W., Jang, H., Seok, J.: Magnetically coupled piezoelectric galloping-based energy harvester using a tandem configuration. Mechanical Systems and Signal Processing. **161**, 107952 (2021) https://doi.org/10.1016/j.ymssp.2021.107952
7. Hu, G., Wang, J., Tang, L.: A comb-like beam based piezoelectric system for galloping energy harvesting. Mechanical Systems and Signal Processing. **150**, 107301 (2021) https://doi.org/10.1016/j.ymssp.2020.107301
8. Tan, T., Hu, X., Yan, Z., Zou, Y., Zhang, W.: Piezoelectromagnetic synergy design and performance analysis for wind galloping energy harvester. Sensors and Actuators A: Physical. **302**, 111813 (2020) https://doi.org/10.1016/j.sna.2019.111813
9. Hu, G., Liang, J., Lan, C., Tang, L.: A twist piezoelectric beam for multi-directional energy harvesting. Smart Mater Struct. **29**(11), 11lt01 (2020) https://doi.org/10.1088/1361-665X/abb648
10. Pan, J., Qin, W., Deng, W., Zhang, P., Zhou, Z.: Harvesting weak vibration energy by integrating piezoelectric inverted beam and pendulum. Energy. **227**, 120374 (2021) https://doi.org/10.1016/j.energy.2021.120374
11. Zhao, L., Tang, L., Yang, Y.: Comparison of modeling methods and parametric study for a piezoelectric wind energy harvester. Smart Mater Struct. **22**(12), 125003 (2013) https://doi.org/10.1088/0964-1726/22/12/125003
12. Rezaei-Hosseinabadi, N., Tabesh, A., Dehghani, R.: A Topology and Design Optimization Method for Wideband Piezoelectric Wind Energy Harvesters. IEEE Transactions on Industrial Electronics. **63**(4), 2165-73 (2015) https://doi.org/10.1109/tie.2015.2499248
13. Hu, G., Wang, J., Su, Z., Li, G., Peng, H., Kwok, K.C.S.: Performance evaluation of twin piezoelectric wind energy harvesters under mutual interference. Appl Phys Lett. **115**(7), 073901 (2019) https://doi.org/10.1063/1.5109457
14. Sun, W., Seok, J.: Novel galloping-based piezoelectric energy harvester adaptable to external wind velocity. Mechanical Systems and Signal Processing. **152**, 107477 (2021) https://doi.org/10.1016/j.ymssp.2020.107477
15. Sun, W., Seok, J.: A novel self-tuning wind energy harvester with a slidable bluff body using vortex-

induced vibration. Energy Convers Manage. **205**, 112472 (2020) https://doi.org/10.1016/j.enconman.2020.112472

16. Zhao, D., Hu, X., Tan, T., Yan, Z., Zhang, W.: Piezoelectric galloping energy harvesting enhanced by topological equivalent aerodynamic design. Energy Convers Manage. **222**, 113260 (2020) https://doi.org/10.1016/j.enconman.2020.113260
17. Zhao, K., Zhang, Q., Wang, W.: Optimization of Galloping Piezoelectric Energy Harvester with V-Shaped Groove in Low Wind Speed. Energies. **12**(24), 4619-36 (2019) https://doi.org/10.3390/en12244619
18. Lee, Y.J., Zhou, G., Lua, K.B.: Two-dimensional numerical study of isotoxal-star polygonal cylinders in cross-flow. Journal of Wind Engineering and Industrial Aerodynamics. **188**, 125-35 (2019) https://doi.org/10.1016/j.jweia.2019.02.020
19. Wang, J., Tang, L., Zhao, L., Zhang, Z.: Efficiency investigation on energy harvesting from airflows in HVAC system based on galloping of isosceles triangle sectioned bluff bodies. Energy. **172**, 1066-78 (2019) https://doi.org/10.1016/j.energy.2019.02.002
20. Zhou, C., Zou, H.-X., Wei, K.-X., Liu, J.: Enhanced performance of piezoelectric wind energy harvester by a curved plate. Smart Mater Struct. **28**(12), 125022 (2019) https://doi.org/10.1088/1361-665X/ab525a
21. Tucker Harvey, S., Khovanov, I.A., Murai, Y., Denissenko, P.: Characterisation of aeroelastic harvester efficiency by measuring transient growth of oscillations. Appl Energy. **268**, 115014 (2020) https://doi.org/10.1016/j.apenergy.2020.115014
22. Yang, K., Qiu, T., Wang, J., Tang, L.: Magnet-induced monostable nonlinearity for improving the VIV-galloping-coupled wind energy harvesting using combined cross-sectioned bluff body. Smart Mater Struct. **29**(7), 07LT1 (2020) https://doi.org/10.1088/1361-665X/ab874c
23. Wang, J., Gu, S., Zhang, C., Hu, G., Chen, G., Yang, K., et al.: Hybrid wind energy scavenging by coupling vortex-induced vibrations and galloping. Energy Convers Manage. **213**, 112835 (2020) https://doi.org/10.1016/j.enconman.2020.112835
24. Yang, X., He, X., Li, J., Jiang, S.: Modeling and verification of piezoelectric wind energy harvesters enhanced by interaction between vortex-induced vibration and galloping. Smart Mater Struct. **28**(11), 115027 (2019) https://doi.org/10.1088/1361-665X/ab4216
25. Sun, W., Jo, S., Seok, J.: Development of the optimal bluff body for wind energy harvesting using the synergetic effect of coupled vortex induced vibration and galloping phenomena. International Journal of Mechanical Sciences. **156**, 435-45 (2019) https://doi.org/10.1016/j.ijmecsci.2019.04.019
26. Lan, C., Tang, L., Hu, G., Qin, W.: Dynamics and performance of a two degree-of-freedom galloping-based piezoelectric energy harvester. Smart Mater Struct. **28**(4), 045018 (2019) https://doi.org/10.1088/1361-665X/ab0852
27. Zhao, L., Tang, L., Yang, Y.: Enhanced piezoelectric galloping energy harvesting using 2 degree-of-freedom cut-out cantilever with magnetic interaction. Jpn J Appl Phys. **53**(6), 060302 (2014) https://doi.org/10.7567/JJAP.53.060302
28. Wang, J., Geng, L., Yang, K., Zhao, L., Wang, F., Yurchenko, D.: Dynamics of the double-beam

piezo–magneto–elastic nonlinear wind energy harvester exhibiting galloping-based vibration. Nonlinear Dynamics. **100**(3), 1963-83 (2020) https://doi.org/10.1007/s11071-020-05633-3

29. Yang, W., Towfighian, S.: Internal resonance and low frequency vibration energy harvesting. Smart Mater Struct. **26**(9), 095008 (2017) https://doi.org/10.1088/1361-665X/aa791d
30. Clementi, F., Lenci, S., Rega, G.: 1:1 internal resonance in a two d.o.f. complete system: a comprehensive analysis and its possible exploitation for design. Meccanica. **55**(6), 1309-32 (2020) https://doi.org/10.1007/s11012-020-01171-9
31. Jiang, W.-A., Ma, X.-D., Han, X.-J., Chen, L.-Q., Bi, Q.-S.: Broadband energy harvesting based on one-to-one internal resonance. Chinese Physics B. **29**(10), 100503 (2020) https://doi.org/10.1088/1674-1056/aba5fd
32. Jiang, W., Han, X., Chen, L., Bi, Q.: Improving energy harvesting by internal resonance in a spring-pendulum system. Acta Mechanica Sinica. **36**(3), 618-23 (2020) https://doi.org/10.1007/s10409-020-00945-4
33. Pu, D., Wei, X., Xu, L., Jiang, Z., Huan, R.: Synchronization of electrically coupled micromechanical oscillators with a frequency ratio of 3:1. Appl Phys Lett. **112**(1), 013503 (2018) https://doi.org/10.1063/1.5000786
34. Cao, D.X., Leadenham, S., Erturk, A.: Internal resonance for nonlinear vibration energy harvesting. The European Physical Journal Special Topics. **224**(14-15), 2867-80 (2015) https://doi.org/10.1140/epjst/e2015-02594-4
35. Sun, W., Guo, F., Seok, J.: Development of a novel vibro-wind galloping energy harvester with high power density incorporated with a nested bluff-body structure. Energy Convers Manage. **197**, 111880 (2019) https://doi.org/10.1016/j.enconman.2019.111880
36. Lan, C., Tang, L., Qin, W., Xiong, L.: Magnetically coupled dual-beam energy harvester: Benefit and trade-off. J Intell Mater Syst Struct. **29**(6), 1216-35 (2017) https://doi.org/10.1177/1045389x17730927
37. Meseguer, J., Sanz-Andrés, A., Alonso, G.: Determination of Maximum Mechanical Energy Efficiency in Energy Galloping Systems. J Eng Mech. **141**(1), 04014101 (2015) https://doi.org/10.1061/(asce)em.1943-7889.0000817
38. Abdelkefi, A., Yan, Z., Hajj, M.R.: Performance analysis of galloping-based piezoaeroelastic energy harvesters with different cross-section geometries. J Intell Mater Syst Struct. **25**(2), 246-56 (2014) https://doi.org/10.1177/1045389X13491019
39. Tang, L., Zhao, L., Yang, Y., Lefeuvre, E.: Equivalent Circuit Representation and Analysis of Galloping-Based Wind Energy Harvesting. IEEE/ASME Transactions on Mechatronics. **20**(2), 834-44 (2015) https://doi.org/10.1109/tmech.2014.2308182
40. Bibo, A., Daqaq, M.F.: An analytical framework for the design and comparative analysis of galloping energy harvesters under quasi-steady aerodynamics. Smart Mater Struct. **24**(9), 094006 (2015) https://doi.org/10.1088/0964-1726/24/9/094006